

**H2020 FET-Open Research and Innovation Actions Project Number 766566  
Antiferromagnetic spintronics (ASPIN)**

**Work package 1, Deliverable D1.3:  
Report on specifications of multi-level antiferromagnetic bit cells  
with electrical writing and readout**

This report summarizes the work of the ASPIN project consortium on determining the specifications of multi-level antiferromagnetic bit cells with electrical writing and readout. We also give references to our corresponding publications containing additional information. The teams’ contributions to this work were as follows:

- Institute of Physics in Prague (IOP): Materials growth and characterization, device fabrication, electrical measurements
- University of Nottingham (NOT): Materials growth and characterization, magnetic imaging
- Max-Planck Institutes (MPG): THz experiments, theory
- IGS Ltd. (IGS): Development of demonstrator printed circuit boards, assessment of application potential
- Charles University in Prague (CHU): Link from electrical and THz measurements to optical measurements
- Johannes Gutenberg University in Mainz (JGU): Theory

**Contents**

<b>1</b>	<b>Overview of writing/read mechanisms and application potential</b>	<b>2</b>
1.1	Initial branch of antiferromagnetic spintronics . . . . .	2
1.2	New branch of antiferromagnetic spintronics . . . . .	2
1.3	Application potential . . . . .	4
<b>2</b>	<b>Cross-shape bit-cells</b>	<b>4</b>
2.1	USB-interfaced printed circuit board . . . . .	4
2.2	Memory-counter . . . . .	6
2.3	Switching pulse lengths in the range of $\sim 10^{-2} - 10^{-10}$ s . . . . .	6
2.4	Heat-assisted switching and temperature-dependent relaxation . . . . .	9
<b>3</b>	<b>Bar-shape bit-cells</b>	<b>10</b>
3.1	Unipolar switching controlled by current amplitude . . . . .	10
3.2	High resistive switching signals . . . . .	12
<b>4</b>	<b>Whetstone-bridge bit-cells</b>	<b>13</b>
4.1	Reproducibility of switching across devices . . . . .	13
4.2	Analog time-dependent switching and relaxation . . . . .	14
4.3	Switching by ns-pulses . . . . .	20
4.4	Switching by strong magnetic fields . . . . .	21
<b>5</b>	<b>Comparison of Whetstone-bridge and cross-shape bit-cells</b>	<b>22</b>

# 1 Overview of writing/read mechanisms and application potential

The initially pursued branch of antiferromagnetic spintronics was based on adapting well established concepts from ferromagnetic spintronics for storing information in different stable orientations of the collective magnetic order vector, writing by current-induced spin-torques, and magnetoresistive readout [1, 2]. While marching in the footsteps of ferromagnetic spintronics, the approach allowed us to demonstrate proof-of-concept memory devices directly showcasing the anticipated comparative advantages of antiferromagnets, including their insensitivity to magnetic fields and absence of stray fields, and the fast THz-scale spin dynamics [3, 4, 5]. It also inspired opening an unexpected chapter of research of topological magneto-transport phenomena [6, 7, 8]. In contrast, the new branch of antiferromagnetic spintronics starts from identifying the weaknesses of the first-generation devices, namely their small readout signals and the writing mechanism limited to only a special type of antiferromagnetic structures [3, 9]. The new paradigm based on quenching the antiferromagnet into metastable nano-fragmented domain states remedies these weaknesses [10] and, moreover, opens possibilities with no counterparts in any of the earlier developed spintronics concepts. The prime example here is the universality of the new switching mechanism, which is applicable from dc to fs-laser pulses and thus bridges spin electronics and ultrafast opto-spintronics by the same underlying operation principle [10]. The availability of both electrical and optical modes of switching also implies that the new concept is in principle applicable to the entire family of antiferromagnets, including metals and insulators. This significantly enlarges the materials playground for spintronics since antiferromagnets are much more abundant than ferromagnets.

## 1.1 Initial branch of antiferromagnetic spintronics

The current-induced writing mechanism considered in first antiferromagnetic memory devices was based on extending the established relativistic spin-orbit torque in ferromagnets with global inversion symmetry breaking to the staggered spin-orbit torque in special antiferromagnetic lattices with local symmetry breaking [9, 3, 2]. Readout was due to anisotropic magnetoresistance (AMR) which was used already in the first generation of ferromagnetic random access memories (MRAMs). The memory effect, again in analogy to ferromagnets, results from switching between ground states with different directions of the collective magnetic order vector. Consistent with this picture, X-ray magnetic linear dichroism - photoemission electron microscopy (XMLD-PEEM) showed reproducible, reversible, and stable switching of large, micron-scale antiferromagnetic domains, controlled by the polarity of the writing current of amplitude  $\sim 10^6 \text{ Acm}^{-2}$  [11]. However, several fundamental limitations have emerged from these initial approach: First, only a couple of antiferromagnets (CuMnAs and  $\text{Mn}_2\text{Au}$ ) have been identified to meet the stringent local symmetry breaking conditions for the staggered spin-torque writing [9, 3, 12, 2]. Second, switching between two ground state magnetic vector directions gives, in principle, only weak relativistic readout signals in single-layer single-domain magnets; for example, AMR is only  $\sim 0.1 \%$  in CuMnAs, as confirmed by Néel vector reorientation experiments using electrical switching or strong magnetic fields [3, 13]). On the other hand, giant-magnetoresistive multilayers, which made ferromagnetic spintronics a commercially viable technology, have not been realized in antiferromagnets. Third, the current-induced spin-torque principle offers no counterpart in optics, i.e., cannot be extended to the ultra-fast switching limit.

## 1.2 New branch of antiferromagnetic spintronics

**Microscopy** using XMLD-PEEM and scanning NV-diamond technique has recently allowed us to identify the new pulse-induced switching mechanism to nano-fragmented domain states in CuMnAs at current amplitudes  $\sim 10^7 \text{ Acm}^{-2}$  [10, 14]. Realizing these imaging experiments in an antiferromagnet in combination with electrical pulsing required us to push the imaging techniques beyond the earlier demonstrated capabilities. Still, their resolution only reached  $\approx 50 \text{ nm}$  while, from the data modelling, the estimates of the feature sizes in the nano-fragmented states were  $\lesssim 10 \text{ nm}$  [14]. This calls for further development of antiferromagnetic microscopies with atomic resolution.

**Readout** signal corresponding to the quenched nano-fragmented domain state in our devices has reached giant-magnetoresistance-like amplitudes ( $\sim 10 - 100\%$ ) in the simplest geometry of a single-layer bar-resistor [10, 14]. This is in contrast to ferromagnets where giant-magnetoresistance signals are achieved only when reversing the collective magnetization vector and at the expense of introducing complex multi-layer structures [15]. A plausibility check for the high resistivity switching amplitudes in the simple antiferromagnetic film was provided by ab initio transport calculations in CuMnAs [16]. Here a relative increase of the resistivity by over 100% was obtained when comparing the resistivity of a material with a perfect antiferromagnetic order to a material with a strong frozen magnetic disorder. We have also demonstrated the optical reflectivity counterpart of the electrical resistivity readout [10].

**Writing** information into the quenched nano-fragmented domain states lifted the stringent limitations of the initial approach based on the Néel vector reorientation by the staggered current-induced torque. The fact that the new mechanism is unrelated to the current-induced spin-torque principle has been both evidenced by and allowed for optical writing [10]. Using the same concept, material, and device we have demonstrated electrical/optical writing scaled from dc down to a single fs-laser pulse in the compensated antiferromagnet CuMnAs. We have demonstrated deterministic polarity/polarization independent electrical/optical switching controlled by the pulse amplitude (see Fig. 1c). This is in stark contrast to the earlier established mechanisms of all-optical switching of the collective magnetization vector in ferrimagnets or ferromagnets [17] which, naturally, are unrelated to the electrical switching by the current-induced spin-torque. Moreover, only ferrimagnets with unequal demagnetization dynamics of the opposite moments were argued to be switchable by a single fs-laser pulse, excluding the abundant family of antiferromagnets. (Note that recent demonstrations of all-optical switching in ferromagnets required, besides demagnetization, multiple circularly-polarized pulses.) We point out that opening the possibility to bridge electrical and optical switching with a unifying mechanism has not been achieved at the expense of excessive pulsing amplitudes; for a ns electrical pulse, the current amplitudes are lower than in experiments in ferromagnetic spin-orbit torque devices [18] and for switching by a fs-laser pulse, our energy is lower than in earlier all-optical switching experiments in ferrimagnets [17]. Another crucial information we have obtained from these switching measurements is that the heating reached during the writing pulse is in the vicinity of the antiferromagnetic transition temperature in CuMnAs ( $T_N = 480$  K), in analogy to all-optical switching of ferrimagnets and ferromagnets.

**Memory** characteristics of the nano-fragmented memory states have allowed us to realize multi-level analog devices with smooth and tunable time-dependence of the relaxation of a universal Kohlrausch stretched-exponential form [10]. In contrast, devices based on switching between ground states with different directions of the collective magnetic order vector are commonly digital (bistable) and the memory loss takes a form of stochastic fluctuations between the two states. The accurate fit of our readout signals by the Kohlrausch model of relaxation in complex systems is, on one hand, fully consistent with the direct images of the complex nano-fragmented domain states observed by the above magnetic microscopies. Simultaneously, the Kohlrausch relaxation is an example, noted in the past in a range of physical systems [19], that reproducible and universal behavior can transcend the details of the complex disordered materials and of the measurement probes. Indeed, we have observed high reproducibility of the above switching characteristics across different physical samples and experimental set-ups. The inferred Kohlrausch exponent corresponds to a diffusion equation describing the relaxation process in 3D. Since measured on 50 nm thick CuMnAs films, this observation is consistent with the domain fragmentation reaching a 10 nm scale. The inferred picosecond relaxation attempt time, corresponding to the dynamics time-scales in antiferromagnets, is another key characteristics of the metastable state that we have identified. This call for future development of antiferromagnetic microscopies with atomic-spatial and fs-temporal resolutions.

**Structural characterization** is an important complement to the above electrical, optical, and magnetic measurements. Several papers have recently reported parasitic pulse-induced resistive changes in metal/antiferromagnetic-insulator bilayers with few-nm thick metal films [20, 21, 22, 23, 24, 25]. These parasitic signals, typically of a fraction of per cent amplitude, are linked to the well-established electromigration effects promoted at grain boundaries in microwires of sputtered thin metal films

[26]. The possible occurrence of parasitic effects highlights the importance of direct imaging of the magnetic switching in the antiferromagnet. In our CuMnAs samples, the magnetic transition to the metastable nano-fragmented domain states has been firmly established by the XMLD-PEEM and NV-diamond microscopies. In complementary structural characterizations [27] we have shown that our single-crystal CuMnAs layers grown by molecular beam epitaxy with the best substrate matching, stoichiometry, uniformity, and minimized abundance of defects have optimized characteristics of the resistive switching signals. X-ray absorption PEEM, X-ray diffraction, scanning electron microscopy, and transmission electron microscopy measurements have confirmed no signs of electromigration or structural transitions of the CuMnAs epilayers for currents and heating conditions corresponding to the high resistive switching experiments [27, 10].

### 1.3 Application potential

The application potential of our new branch of antiferromagnetic spintronics can be already expected in areas including spiking neural circuits for which no commercially viable analog memory technology exists to date. On the experimental spintronics side, there is only one other alternative magnetic memory concept considered for spiking neuromorphics [28]. Here, however, the time-dependence is realized via the extrinsic transient heating by the pulses. This is fundamentally distinct from our mechanism relying on the intrinsic smooth, universal and tunable relaxation from the higher energy metastable states. We emphasize that we do not expect an immediate technological impact of our results. For example the existing commercial ferromagnetic or phase change memory chips have been developed over decades, preceded by decades of related materials research into magnetic or optical storage media. Antiferromagnetic memories have emerged as a research field only in 2016. And while their first principle of operation could still be linked to the principle of the mature ferromagnetic memories, the new mechanism explored is unparalleled. This level of novelty virtually excludes any realistic prospect of an immediate technological impact. It is also beyond the scope of this project to make a cross-platform comparison between our devices and non-magnetic resistive memories. In general, both magnetic and non-magnetic resistive memories are considered as viable candidates to complement semiconductor memories and the cross-platform benchmarking is another complex multi-disciplinary task on its own.

## 2 Cross-shape bit-cells

In the first and second part of this section we focus on the response of cross-shape CuMnAs bit-cells to electrical pulses in the microsecond to millisecond range [4]. To highlight the realistic prospect of transferring our concept of the electrical control of antiferromagnets (AFs) from laboratory experiments to future practical IoT applications, we start in the first part by describing our implementation of the multi-level CuMnAs bit-cell in a standard printed circuit board (PCB). In the following part we present systematic data on the memory-counter characteristics as a function of the pulse length, duty cycle, and integrated pulse-time. In the third part of this section we extend the measurements to pulse lengths scaled down to a  $\sim 100$  ps range [4]. These are the limiting pulse lengths accessible electrically and we demonstrate a reproducible memory-counter functionality with  $\sim 1000$  pulses. All combined, our cross-shape micron-size bit cells can act as a multi-level memory-counter over the entire range of electrical pulse lengths downscaled to  $\sim 100$  ps.

### 2.1 USB-interfaced printed circuit board

Figures 1 and 2 provide an overview of the basic characteristics of our AF CuMnAs cross-shape memory cells. Here the cell,  $2 \mu\text{m}$  in size (Fig. 1b), is patterned by electron beam lithography and reactive ion etching from a 60 nm thick, single-crystal CuMnAs film (Fig. 1a). The material shown here was grown by molecular beam epitaxy (MBE) on a GaP substrate [29]. We recall that, besides basic research, MBE is widely used in the manufacture of microelectronic devices, in particular for mobile

technologies. We also note that GaP is lattice matched to Si and that, as shown below, high quality CuMnAs films can be deposited on both GaP and Si at temperatures between 220 and 300°C, i.e., well below the CMOS circuit tolerance limit which is typically above 400°C. Our CuMnAs films are metallic with a conductivity of  $5\text{--}8 \times 10^3 \Omega^{-1}\text{cm}^{-1}$ . The cell write/read signals can be sent at ambient conditions using a standard digital PCB, connected to a personal computer via a USB interface (Fig. 1c).

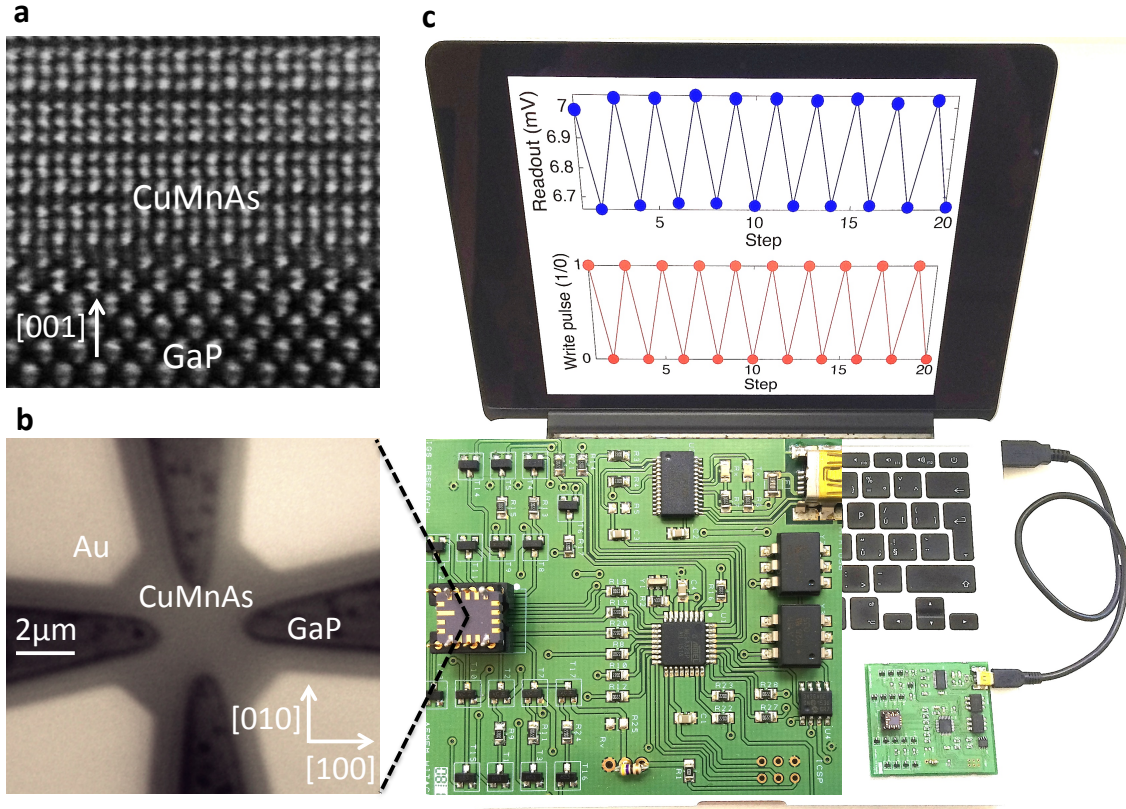


**Figure 1: AF CuMnAs bit cell with microelectronic compatibility.** (a) Scanning transmission electron microscopy image in the [100]-[001] plane of the CuMnAs epilayer grown on a GaP substrate. (b) Optical microscopy image of the device containing Au contact pads (light) and the AF CuMnAs cross-shape bit cell on the GaP substrate (dark). (c) Picture of the PCB with the chip containing the AF bit cell and the input write-pulse signals (red dots) and output readout signals (blue dots) send via a USB computer interface.

Writing current pulses delivered using the four contacts of the bit-cell are depicted by red arrows in Fig. 2a. Electrical readout is performed by running the probe current along one of the arms of the cross (blue arrow in Fig. 2a) and by measuring the AF transverse resistance across the other arm [3, 30]. The simplicity of the circuitry sufficient to operate the AF bit-cell is highlighted in Fig. 2b. Apart from the CuMnAs memory chip it contains only standard transistors and an Arduino microcontroller, powered by a 5 V USB 2.0 socket, for sending the write/read voltage signals. The device operates at ambient conditions and shows highly reproducible multi-level switching signals with a single readout step and no additional output data processing.

Examples of different write-pulse sequences and corresponding multi-level readout signals obtained with our proof-of-concept USB device are shown in Figs. 2c,d. In one case a symmetric pulsing was applied, repeating four pulses with current lines along the [100] direction followed by four pulses with current lines along the [010] direction. In the second case, the four pulses with current lines along the [100] direction are followed by fifty pulses with current lines along the [010] direction. The results

illustrate a deterministic multi-level switching of the CuMnAs bit cell.

We now proceed to exploring in detail the dependencies of the readout signals on the parameters of writing pulses. The study presented below involves tens of thousands of switchings with individual pulse lengths spanning eight orders of magnitude from  $\sim 10$  ms down to  $\sim 100$  ps. We performed the experiments using laboratory electrical pulse generators or high frequency set-ups equipped with rf cables and the AF devices mounted on specially designed co-planar waveguide with rf access.

## 2.2 Memory-counter

We first focus on the multi-level bit cell characteristics when written by trains of pulses with the individual pulse length varied from milliseconds to microseconds. The results, summarized in Figs. 3a-d, were obtained using the following measurement protocol: Before each train of pulses (with writing current lines along the [100] direction), the cell was reset to the same initial state. The maximum length of the pulse train, including all pulses and delays between pulses, was set to 100 ms and readout was performed 5 s after the last pulse in the train. The writing current was fixed at 46 mA (corresponding to a current density of  $2.7 \times 10^7$  Acm<sup>-2</sup>) and the readout current was 500  $\mu$ A.

In Fig. 3a we compare the dependencies of the readout signal on the number of pulses for different individual pulse lengths. The dependencies are highly reproducible as indicated by error bars obtained from repeated measurements for each pulse train. The AF bit cell acts as a counter of pulses whose number can be in hundreds. The separation of the readout signals for different numbers of pulses, i.e. the accuracy of the pulse counting, increases with increasing individual pulse length and can reach a single-pulse resolution. The duty cycle was fixed in all measurements shown in Fig. 3a to 0.025. In Fig. 3b we show that for a given individual pulse length, the duty cycle (delay between pulses) can be varied over a broad range without affecting the readout signal of the counter.

In Figs. 3c,d we plot the readout signal dependence on the integrated pulse time, i.e., on the number of pulses multiplied by the individual pulse length. Over a broad range of individual pulse lengths, the dependencies fall onto a universal curve making the AF memory cell a detector of the integrated pulse time, as shown in Fig. 3c. The universal trend breaks down for individual pulse lengths smaller than  $\approx 50$   $\mu$ s. This can be explained by heating assisted spin-orbit torque switching in our devices. By a direct measurement of the heating during the pulse we observe that in the 2  $\mu$ m cells the heating saturates at pulse lengths exceeding tens of  $\mu$ s. For these longer pulses, switching occurs at the saturated temperature which results in the universal dependence of the readout signal on the integrated pulse time. For shorter pulses, the temperature during switching does not reach saturation and the heating decreases with decreasing pulse length which results in the lower readout signal. We note that in all measurements the temperature during switching stays at least 100 K below the CuMnAs Néel temperature ( $T_N = 480$  K)[31].

An accurate detection of the integrated pulse time is feasible for tens of pulses in our measurements, as shown in Fig. 3d. For pulse numbers exceeding one hundred, the readout signal at a given integrated pulse time drops down from the universal trend because of the non-saturated heating during the shorter pulses. The signal reduction gets stronger at lower integrated pulse times with correspondingly smaller individual pulse lengths. For the current density used in the measurements in Fig. 3, the readout signal vanishes for pulse lengths below a microsecond.

## 2.3 Switching pulse lengths in the range of $\sim 10^{-2} - 10^{-10}$ s

Our measurements show that it is possible to switch AF domains using current pulse lengths reaching the limiting,  $\sim 100$  ps scale of electrical generation. In Fig. 4a we plot a typical dependence of the measured readout signal on the length of a single writing pulse. Before each measurement of the given pulse length, the cell was reset to the same initial state and then the single write pulse was applied with the current lines along the [100] direction. The readout signal increases with increasing pulse length. This is analogous to the dependence on the number of pulses and reflects the multi-domain nature of the switching.

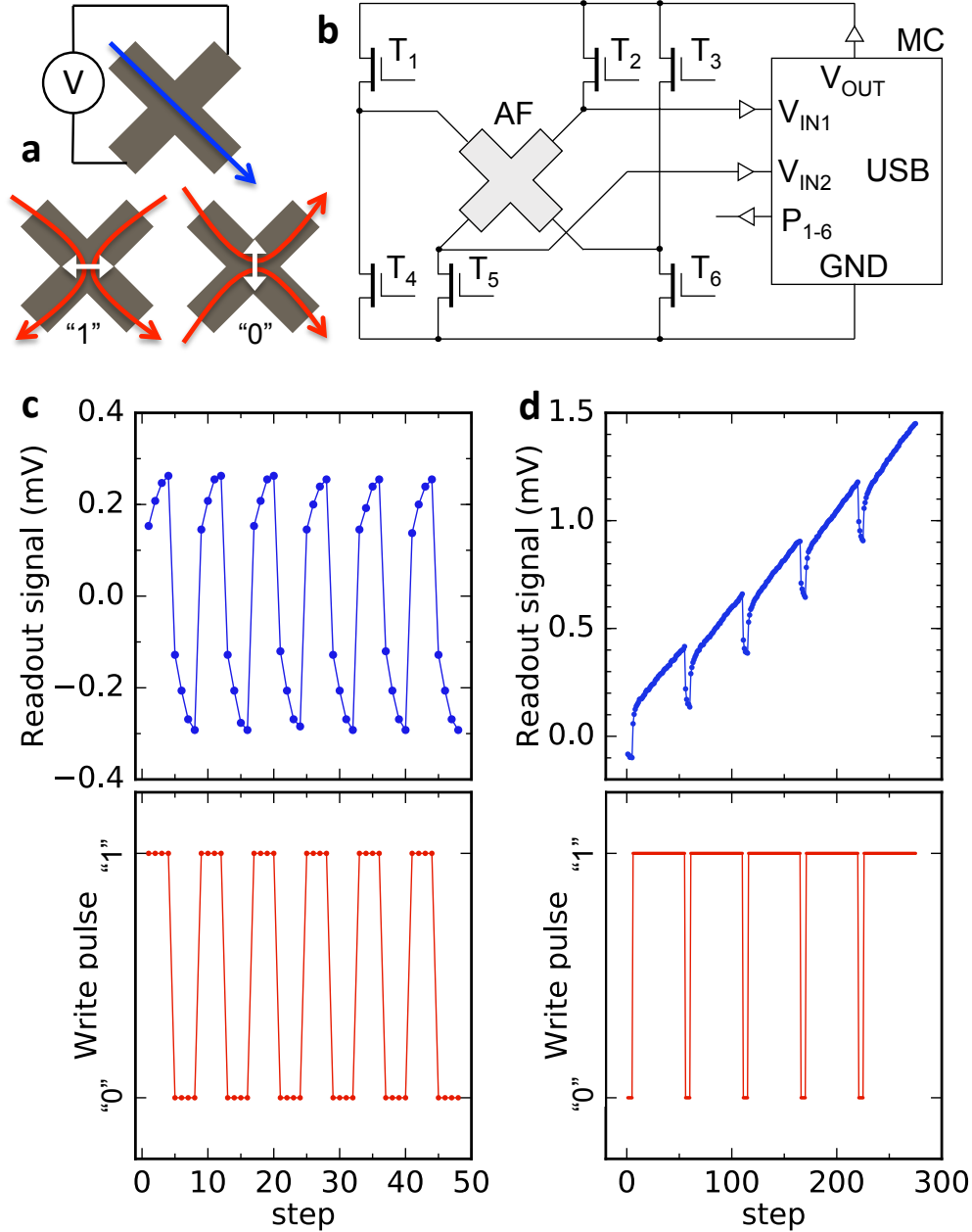


Figure 2: **Multi-level AF memory bit cell.** (a) The readout current (blue arrow) and transverse voltage detection geometry; write pulse current lines (red arrows) labeled "1" and "0" and the corresponding preferred AF moment orientations (white double-arrows). (b) Schematics of the circuitry controlling the write/read functions. Microcontroller (MC) supplies the AF bit-cell circuit through its adjustable voltage output  $V_{OUT}$ ; different writing and reading configurations are realized by switching transistors  $T_1$  to  $T_6$  controlled by digital outputs  $P_1$  to  $P_6$  of the MC; transversal voltage is sensed differentially by analogue voltage inputs  $V_{IN1}$  and  $V_{IN2}$  of the MC. GND labels ground. (c) A symmetric pulsing with repeated four write pulses with current lines along the [100] direction labelled "0" followed by four pulses with current lines along the [010] direction labelled "1" (red dots); corresponding readout signals (blue dots). (d) Same as (c) with the four "0" write pulses followed by fifty "1" pulses. All measurements were performed at room temperature.

The initial linear increase of the readout signal with increasing pulse length defines the signal per pulse length ratio which we plot in Fig. 4b as a function of the writing current density. For comparison,

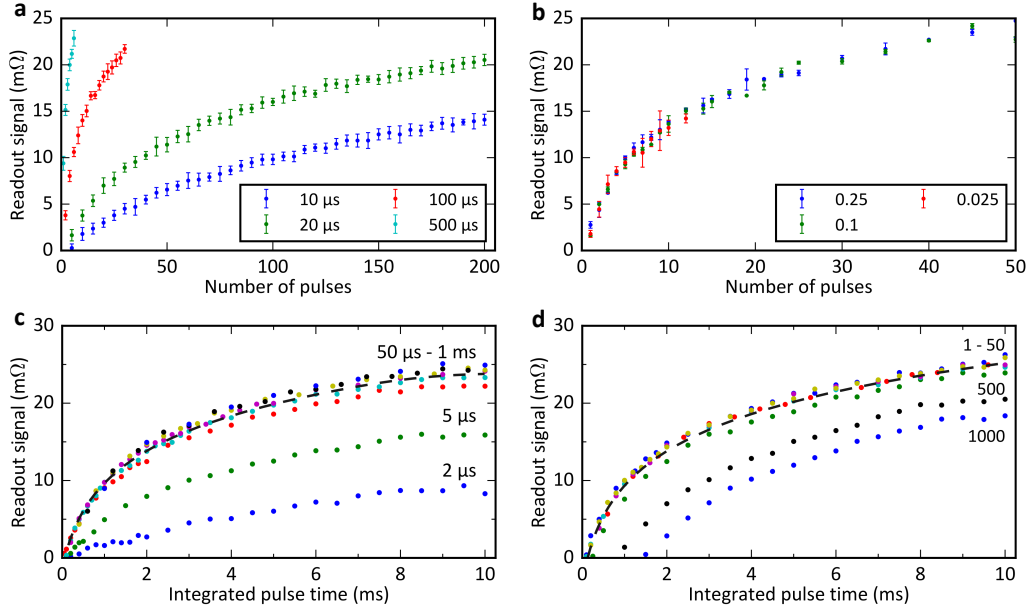


Figure 3: **AF memory-counter bit cell characteristics.** (a) Readout signal as a function of the number of pulses in the train of pulses, for different values of the individual pulse length and a common duty cycle of 0.025. All data points are obtained starting from the same reference state. The writing current density is  $2.7 \times 10^7 \text{ Acm}^{-2}$ . Plotted data points are the average over ten measurements; error bars represent the standard deviation. (b) Same as (a) for different duty cycles (corresponding to different delays between individual pulses) and for a common individual pulse length of  $200 \mu\text{s}$ . (c) Same as (a) measured as a function of the integrated pulse time and plotted for different individual pulse lengths. (d) Same as (c) plotted for different number of pulses in the pulse train. The lines connecting the data points are a guide to the eye. All measurements were performed at room temperature.

we included in the plot data points for a  $30 \mu\text{m}$ -size cell used in measurements with pulse lengths in the range of  $\sim 10^{-2} - 10^{-3} \text{ s}$  reported in Ref. [3], for a  $2 \mu\text{m}$ -size cell described above, and for an additional  $4 \mu\text{m}$ -size cell patterned from a  $50 \text{ nm}$  thick CuMnAs epilayer on a GaAs substrate. The  $30 \mu\text{m}$  cell experiments allowed us to explore only a limited range of current densities before heating damaged the sample. For the  $2 \mu\text{m}$  and  $4 \mu\text{m}$  cells, much higher current densities can be applied which allowed us to scale the writing pulse length from milliseconds[3] down to sub-nanoseconds while keeping the  $\text{m}\Omega$  level of the readout signal, as illustrated in Fig. 4b. The signal per pulse length ratio shows an initial step increase with the current density followed by a much weaker, nearly linear dependence. This is consistent with the thermally activated switching process.

In Fig. 4c, we show memory-counter measurements for individual pulse length of  $250 \text{ ps}$ , i.e., at the limit of pulse lengths accessible by electrical generation. We tested counting up to 1000 pulses and, as in the case of the  $\sim\text{ms}$  and  $\mu\text{s}$  pulses, we observe a highly reproducible monotonic dependence of the readout signal on the number of pulses. Note that for individual data points the error bars were obtained from fifteen independent measurements which also means that the bit cell was exposed to  $\sim 25,000$  writing pulses during this study.

In Fig. 4d that bit-cells fabricated from CuMnAs films deposited on Si at  $220^\circ\text{C}$  also show the highly-reproducible multi-level switching characteristics as the devices fabricated from CuMnAs on GaP or GaAs substrates (cf. Fig. 2). The plot shows an example of a symmetric pulsing experiment of repeating three writing pulses with current lines along the  $[100]$  direction followed by three pulses with current lines along the  $[010]$  direction. The corresponding histogram taken from 300 pulses highlights the deterministic switching of these multi-level cross-shape CuMnAs/Si bit-cells.

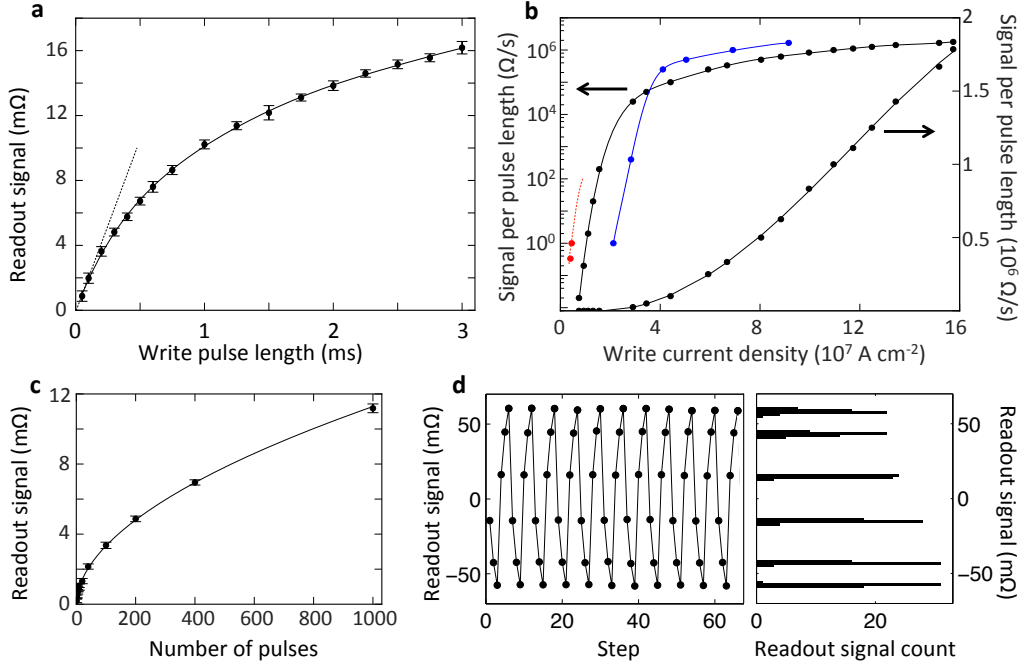


Figure 4: **Dependence on switching pulse-length and bit cells on III-V and Si substrates.** (a) Readout signal of a 4 μm CuMnAs/GaAs device as a function of the applied write-pulse length at a fixed current density of  $1.2 \times 10^7$  Acm $^{-2}$  and current lines along the [100] direction. Reading is performed with a current density of  $5 \times 10^5$  Acm $^{-2}$ , 5 s after the write pulse. The initial linear slope of the dependence (signal per pulse length ratio) is highlighted by the dashed-line linear fit. Plotted data points are the average over fifteen measurements; error bars represent the standard deviation. (b) Readout signal per write-pulse length obtained from the initial linear slope (see panel a) as a function of the write current density, for 30 μm CuMnAs/GaP (red), 4 μm CuMnAs/GaAs (black), and 2 μm CuMnAs/GaP (blue) devices. (c) Readout signal as a function of the number of pulses in the train of pulses for the individual pulse length of 250 ps and writing current density  $16 \times 10^7$  Acm $^{-2}$  in a 4 μm CuMnAs/GaAs devices. All measurements were performed at room temperature. Plotted data points are the average over fifteen measurements; error bars represent the standard deviation. (d) Multi-level switching in the device fabricated from CuMnAs/Si. Three pulses are applied along the [100] direction followed by three pulses along the [010] direction with current density of  $2 \times 10^7$  Acm $^{-2}$  and pulse length 100 μs. Right: Histogram of the six different states, obtained from 50 repetitions of the 3+3 pulse sequence (bin size is 1.4mΩ).

## 2.4 Heat-assisted switching and temperature-dependent relaxation

In the left panel of Fig. 5 we show an example of temperature evolution determined from resistance measured during a 100 μs long writing pulse. We observe fast increase of the temperature in the first  $\sim 10$  μs followed by a saturated regime. This saturation of temperature is connected with establishing thermal gradient in the substrate below the device resulting in an effective heat outflow. The right panel of Fig. 5 shows the current density needed to write a 5 mΩ signal and the temperature  $T_{end}$  of the device at the end of the pulse, both as a function of the base temperature  $T_{base}$ . The current density increases significantly with decreasing base temperature while the temperature at the end of the pulse is similar. This highlights the heat-assisted nature of the reversible switching in our devices. It is also consistent with the observed saturation of the writing energy at shorter pulses during which heat does not have time to dissipate from the device. In this regime the transient increase of sample temperature during the pulse can be expected to scale with the delivered energy.

In Fig. 6 we show switching experiments with trains of 100 μs pulses and subsequent relaxation at

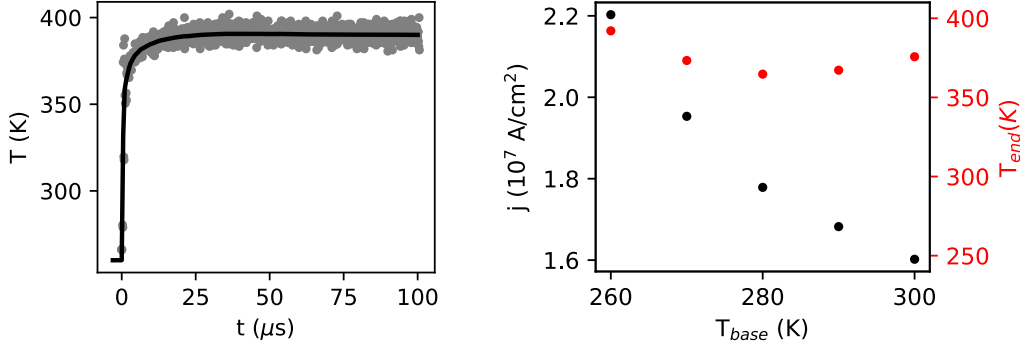


Figure 5: Device temperature with the pulse on. Left panel: An Example of the evolution of the temperature of the device determined from resistance measurements during a 100  $\mu\text{s}$  long writing pulse of current density  $2.2 \times 10^7 \text{ Acm}^{-2}$  and base temperature 260 K. Right panel: Current density (black) needed to write a 5 m $\Omega$  signal and temperature of the device at the end of the writing pulse (red) as a function of the base temperature.

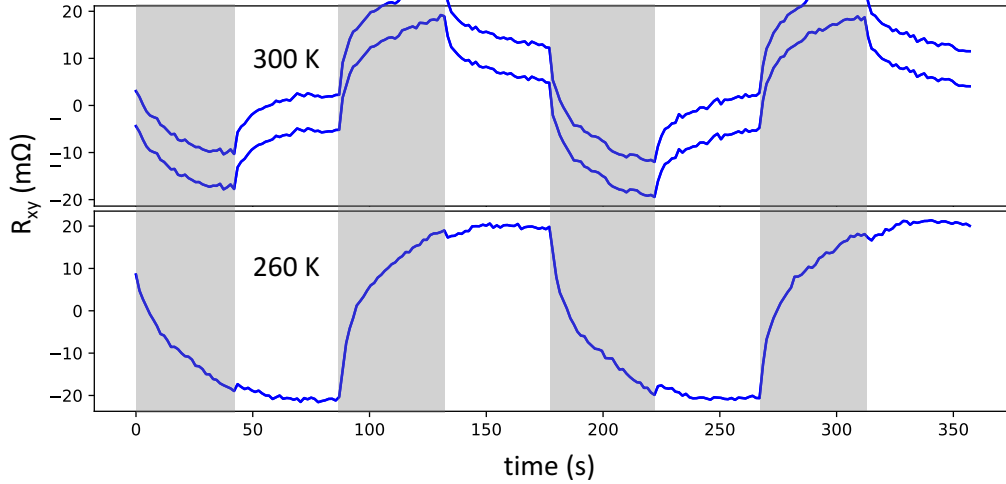


Figure 6: Comparison of switching at 300 K and 260 K. Examples of switching by trains of 30 pulses within 45 s with individual pulse-length of 100  $\mu\text{s}$  and alternating orthogonal writing current directions (grey regions), and of signal relaxation within 45 s with the pulse-train turned off (light regions) at (A) base temperature 300 K and writing current density  $1.6 \times 10^7 \text{ Acm}^{-2}$  and (B) base temperature 260 K and writing current density  $2.2 \times 10^7 \text{ Acm}^{-2}$ .

300 K and 260 K measured in the same CuMnAs structure as in Fig. 3. While at room temperature we observe partial relaxation of the signal, no relaxation is observed in this CuMnAs structure already when slightly lowering the temperature to 260 K.

### 3 Bar-shape bit-cells

#### 3.1 Unipolar switching controlled by current amplitude

In Fig. 7 we present results of the switching by unipolar electrical current pulses in a bar resistor. Our microdevices (see Fig. 7b) were lithographically patterned from a 50 nm thick epilayer of tetragonal CuMnAs of 20  $\Omega$  sheet resistance grown by molecular beam epitaxy on an insulating lattice-matched GaP substrate (see Fig. 1a) [29, 27]. In the measurements plotted in Fig. 7c we use the simplest

two-point resistor geometry for delivering the writing pulses and for detecting the readout signals. We start by applying a  $100\ \mu\text{s}$  long electrical writing pulse and measure for 1 s the resulting change in the ohmic resistance of the device. The experiment is performed at room temperature. The pulse switches the device into a metastable high resistance state. Next we apply a  $100\ \mu\text{s}$  writing pulse of the same polarity and of amplitude reduced by 8% compared to the first writing pulse, and again detect the change in the resistance. This time, the resistance drops back towards the low relaxed value. This switching pattern is precisely reproducible, as illustrated in Fig. 7c on an example of ten high/low resistance switching sequences. A different pulsing sequence confirming the reproducible and deterministic switching characteristics is shown in Fig. 8.

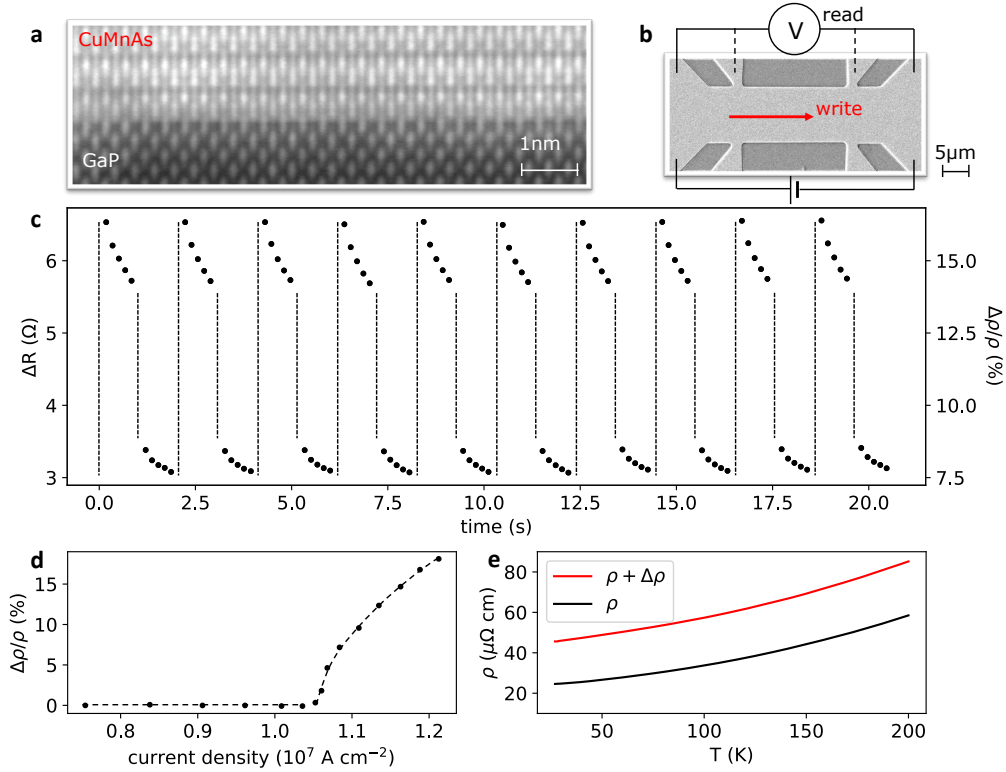


**Figure 7: Unipolar high resistive switching in an elementary bar resistor microdevice.** **a**, TEM micrograph [27] of the single-layer CuMnAs antiferromagnet deposited on an insulating GaP substrate. **b**, SEM micrograph of the microbar device and schematics of the measurement set-up. Solid/dashed voltage probes correspond to the two/four-point readout measurement. **c**, Two-point measurement of alternating switching between higher and lower resistance metastable states at room temperature. The higher resistance state is written by a current amplitude of  $1.2 \times 10^7\ \text{A cm}^{-2}$ . The lower resistance state is written by a current pulse of a 8% weaker amplitude. The electrical pulses have the same polarity and are  $100\ \mu\text{s}$  long. **d**, Four-point measurement of the resistivity switching ratio as a function of the current density at room temperature. Dashed lines in **c,d** are guides to the eye. **e**, Electrical switching is performed at 200 K and then the temperature dependence of the resistivity after switching ( $\rho + \Delta\rho$ ) is compared to the temperature dependence of the resistivity without applying the switching pulse ( $\rho$ ).

The resistance drop after the weaker pulse excludes the possibility that the detected high resistance after the first pulse was due to the sample still remaining at an elevated temperature during the 1 s readout time. In Fig. 9 we show that within a few  $\mu\text{s}$  after the pulse, the sample cools down back to the base temperature. Our switching signals are therefore detected at times safely exceeding the transient heating time. We estimated from the measured resistivity during the  $100\ \mu\text{s}$  pulse that the temperature of the device reaches approximately  $200 \pm 50^\circ\text{C}$ , i.e., is around the CuMnAs Néel

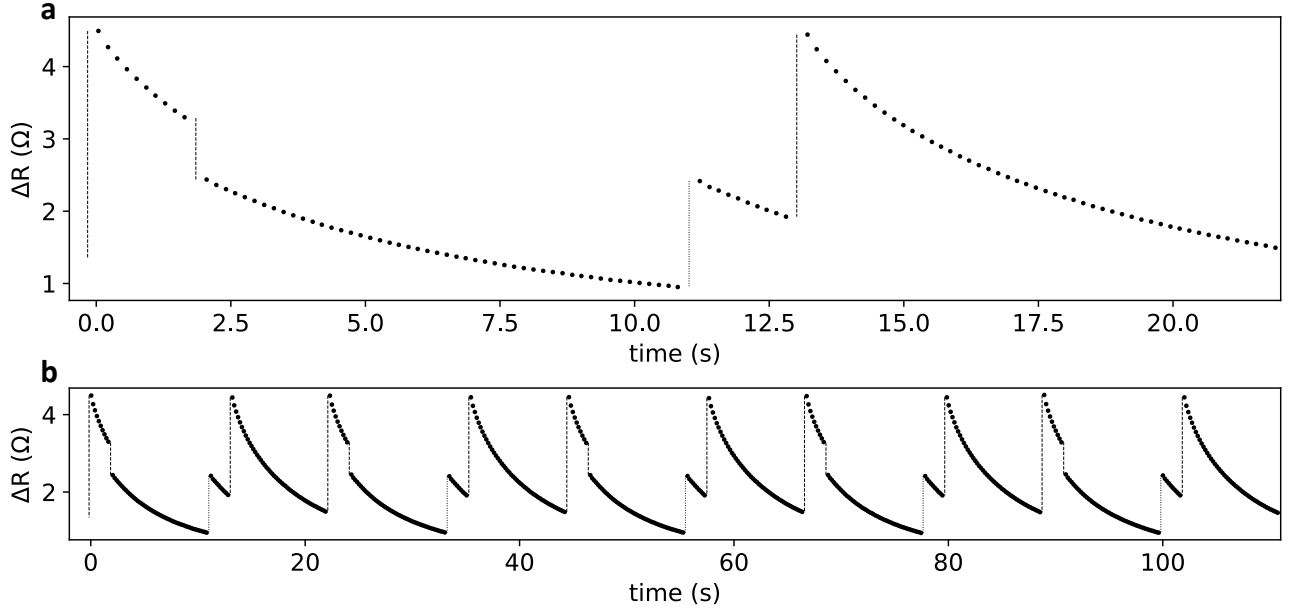


Figure 8: **a**, A sequence of switching to high/low/low/high resistance states at room temperature in the microbar device (Fig. 2b in the main text). The higher resistance state is written by a current amplitude of  $1.13 \times 10^7 \text{ Acm}^{-2}$  (corresponding to 7.1 V voltage drop between the  $20 \mu\text{m}$  spaced voltage probes). The lower resistance state is written by a  $1.08 \times 10^7 \text{ Acm}^{-2}$  current pulse (6.4 V). The current pulses have the same polarity and are  $100 \mu\text{s}$  long. **b**, Same as **a**, with the high/low/low/high sequence repeated five times.

temperature [29].

In Fig. 7d we plot the relative size of the switching signal,  $\delta\rho/\rho$ , obtained directly from a four-point resistivity measurement (see dashed voltage probes in Fig. 7b). The data are plotted for amplitudes of the writing pulses safely below any detectable parasitic electromigration effects. In all electrical pulsing experiments we use a voltage pulse-source. The voltage-current characteristics for the  $100 \mu\text{s}$  writing pulse is shown in Fig. 9. In Fig. 7d we see no switching signal at lower current amplitudes and an onset followed by an increase with increasing pulse amplitude. In all measurements, the reading current amplitude is well below the onset writing current. The resistive switching ratio approaches 20% at room temperature, i.e., is comparable to the giant-magnetoresistance ratios in ferromagnetic multilayers [15].

### 3.2 High resistive switching signals

While at 300 K the metastable high-resistive state relaxes within a  $\sim 10 \text{ s}$  time-scale, at 200 K the relaxation time approaches a year (for details see the discussion of Fig. 19). When switching the device by the  $100 \mu\text{s}$  writing pulse at 200 K we can therefore perform longer measurements, such as the temperature sweep shown in Fig. 7e, with no relaxation of the written high-resistive state. By comparing the temperature dependence of the resistivity after applying the writing pulse,  $\rho + \delta\rho$ , to the resistivity without the pulse,  $\rho$ , we see that the switching signal  $\delta\rho$  is nearly temperature independent while  $\rho$  decreases with decreasing temperature in the metallic CuMnAs. As a result, the switching ratio approaches 100% at low temperatures. We point out that the simple bar-geometry of our devices and their micron-scale size were chosen to highlight the bulk resistivity nature of our switching signals. A comparison of CuMnAs films with thicknesses between 50 and 20 nm further verifies that the signal stems from the bulk of the antiferromagnetic metallic film and not from interface or surface effects.

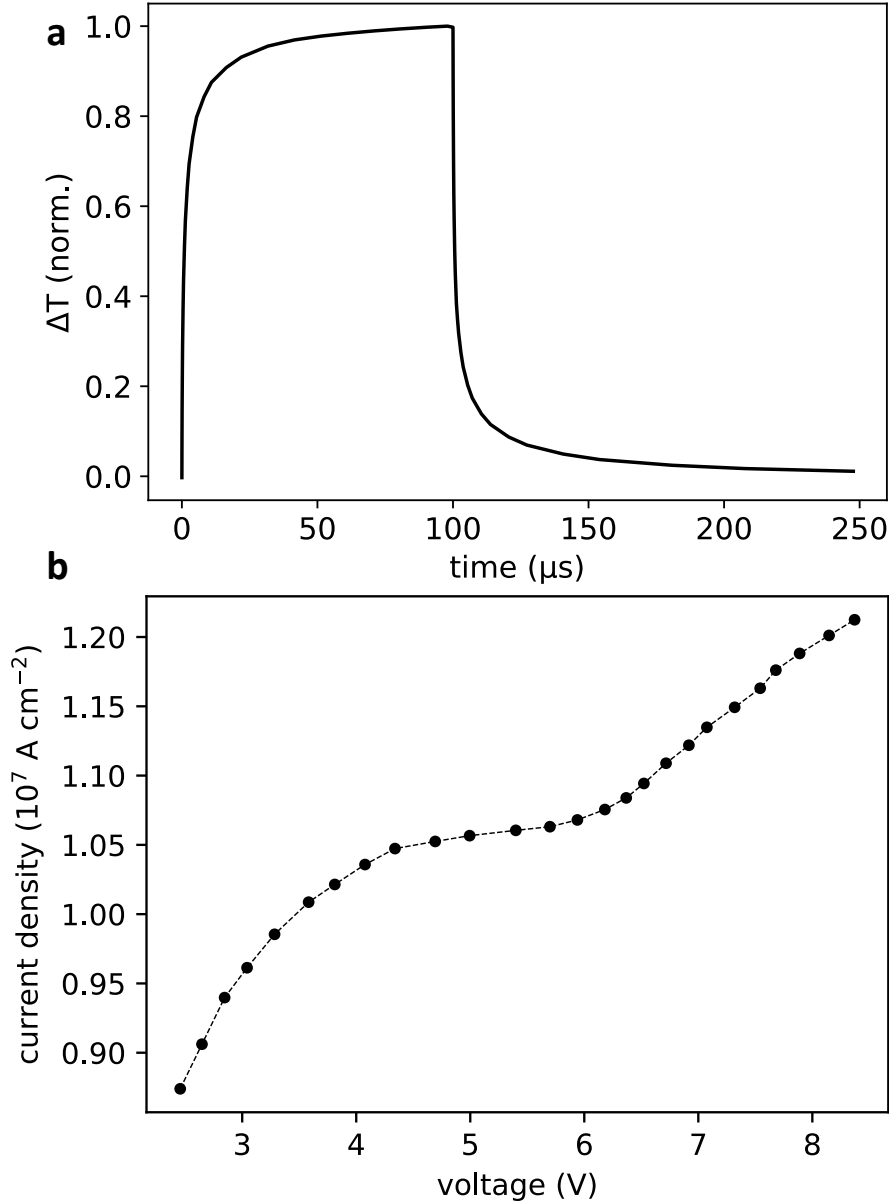


Figure 9: **a**, Comsol simulation of the time dependence of the relative temperature rise during the 100  $\mu s$  writing pulse and of the decay after the pulse. **b**, Pulsing current-voltage characteristics of the microbar device with the voltage measured between the 20  $\mu m$  spaced voltage probes (see Fig. 7b).

## 4 Whetstone-bridge bit-cells

### 4.1 Reproducibility of switching across devices

In Fig. 10 we show measurements on a Wheatstone-bridge microdevice which brings several technical advantages over the simple bar geometry. By pulsing the bridge first along one pair and then along the orthogonal pair of resistors and by measuring the bridge resistance  $R_T$  (Fig. 10a) we can directly check the reproducibility of the switching signal between different physical resistors while using the same readout probes. Apart from the flipped sign of  $R_T$ , which is a geometry effect of the Wheatstone-bridge, the two pairs of resistors show a quantitatively identical switching pattern, as seen in Fig. 10b. This includes the increase of the switching signal with the number of successive pulses of the same amplitude, and the relaxation after each pulse (for more examples see Figs. 11-15).

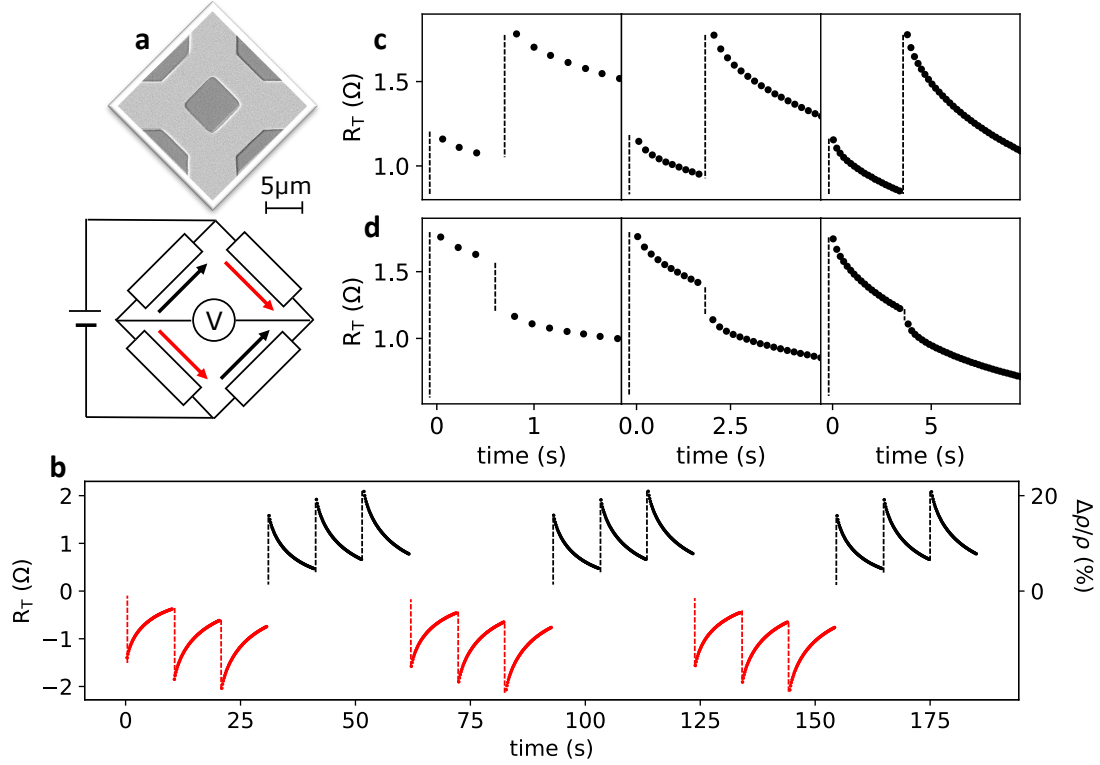


Figure 10: **Reproducible analog switching characteristics.** **a**, SEM micrograph of the Wheatstone-bridge device and schematics of the electrical writing applied along one pair of resistors (red arrows) and the orthogonal pair of resistors (black arrows). In the bridge readout set-up, the readout current is applied between two corners of the bridge (battery sign) and the voltage is measured between the other two corners (voltmeter sign). **b**, Switching signal measured across the bridge for three successive writing pulses of the same amplitude delivered along one pair of arms (red arrows in **a**), followed by three successive writing pulses of the same amplitude along the other pair of arms (black arrows in **a**). **c**, Lower/higher switching sequence for 9.5/10.5 V writing electrical pulses applied across the respective arms of the Wheatstone device (pulse-voltage includes the contact resistance contribution). The three panels correspond to three different delays between the lower and higher writing pulse. **d**, Same as **c**, for the reversed order of the two pulses.

## 4.2 Analog time-dependent switching and relaxation

Figs. 10c,d further highlight the analog time-dependent characteristics of our switching signals. When the successive writing pulses have different amplitudes, the written signal can encode the order and delay between the pulses. The presence of a falling edge indicates that the weaker pulse arrived after the stronger pulse and the size of the falling edge decreases with increasing the delay between the two pulses. Figs. 16,17 highlight the reproducibility and show a more systematic mapping of this analog time-dependent characteristics. We point out that highly reproducible switching characteristics are obtained for different CuMnAs wafers prepared under equivalent growth conditions, and similar switching behavior is also seen in films grown on GaAs or Si over a range of growth parameters [27], and in different device geometries (cf. Fig. 7, Fig. 8, Fig. 10, Fig 11-18).

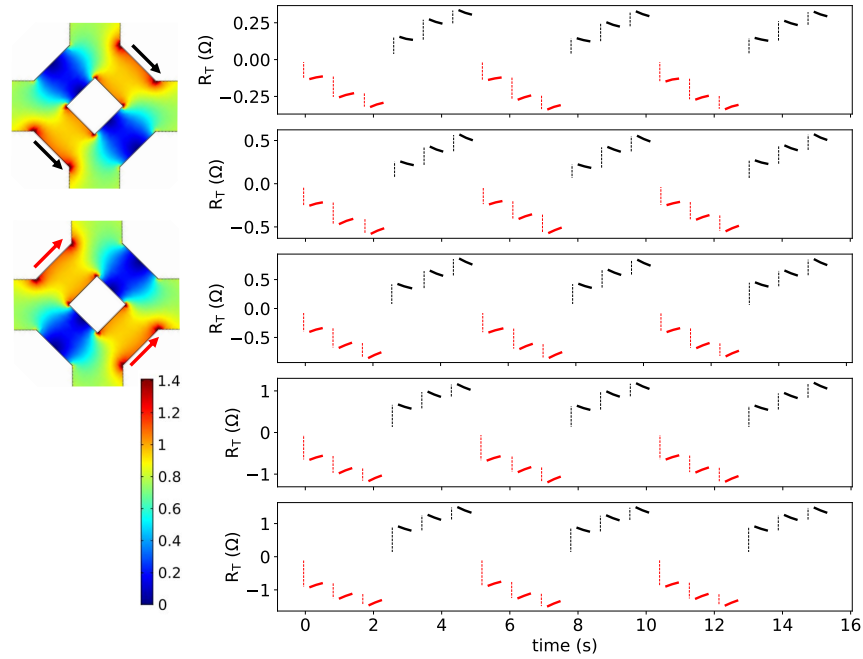


Figure 11: Left: Comsol simulation of the writing current density map in the Wheatstone bridge device. Right: Switching signal measured across the bridge for three successive writing pulses of the same amplitude delivered along one pair of arms (red arrows in the left panel) followed by three successive writing pulses of the same amplitude along the other pair of arms (black arrows in the left panel). From top to bottom the voltage applied during the pulse across the respective arms (including the contact resistance contribution) is 9–11 V. The delay between successive pulses is 0.8 s. The experiments were done at room temperature.

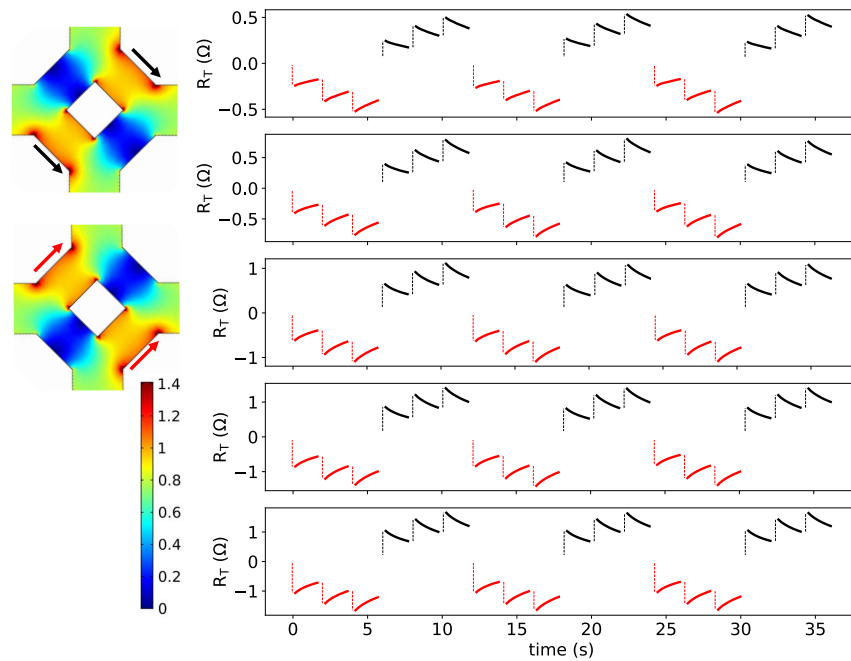


Figure 12: Same as Fig. 11 for the delay between pulses of 2 s.

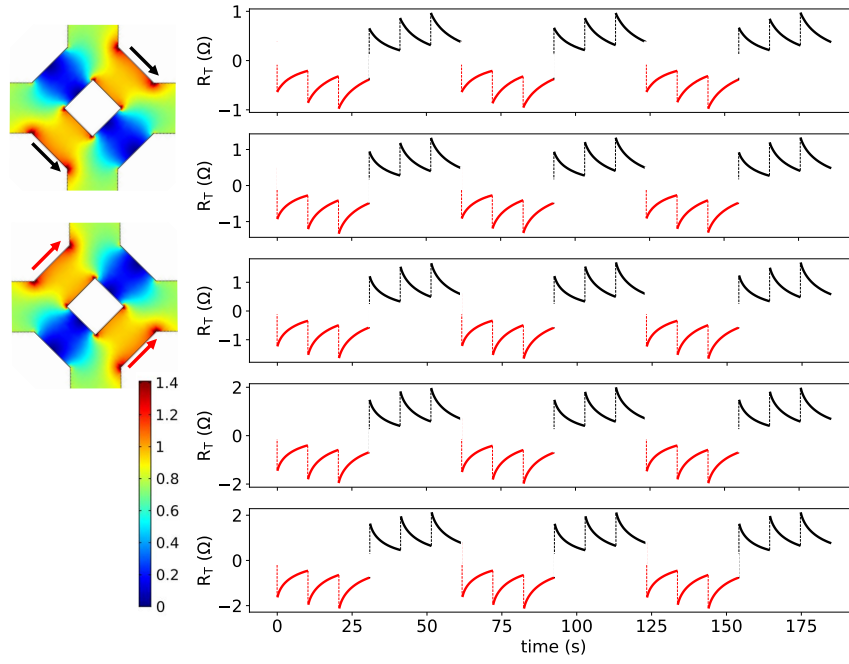


Figure 13: Same as Fig. 11 for the delay between pulses of 10 s.

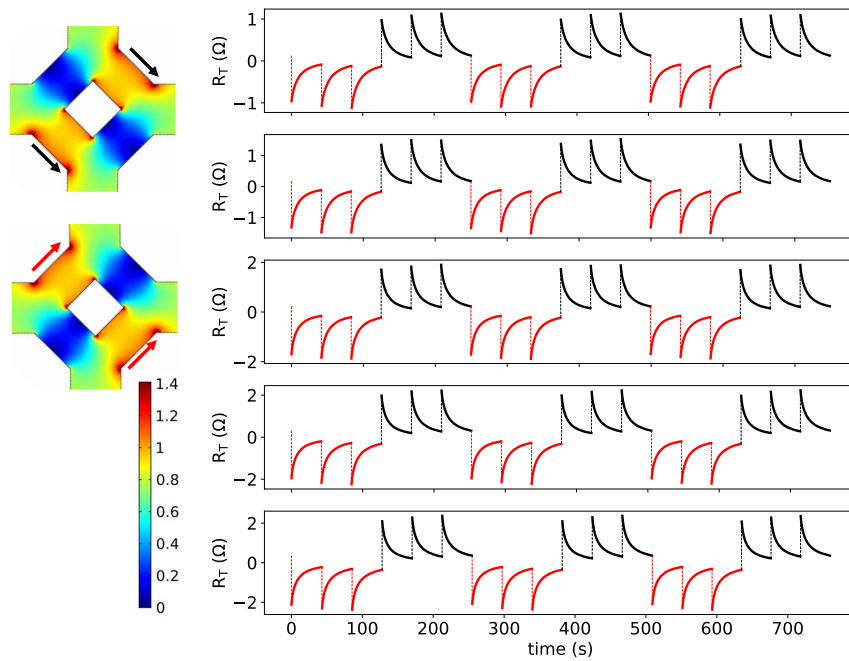


Figure 14: Same as Fig. 11 for the delay between pulses of 41 s.

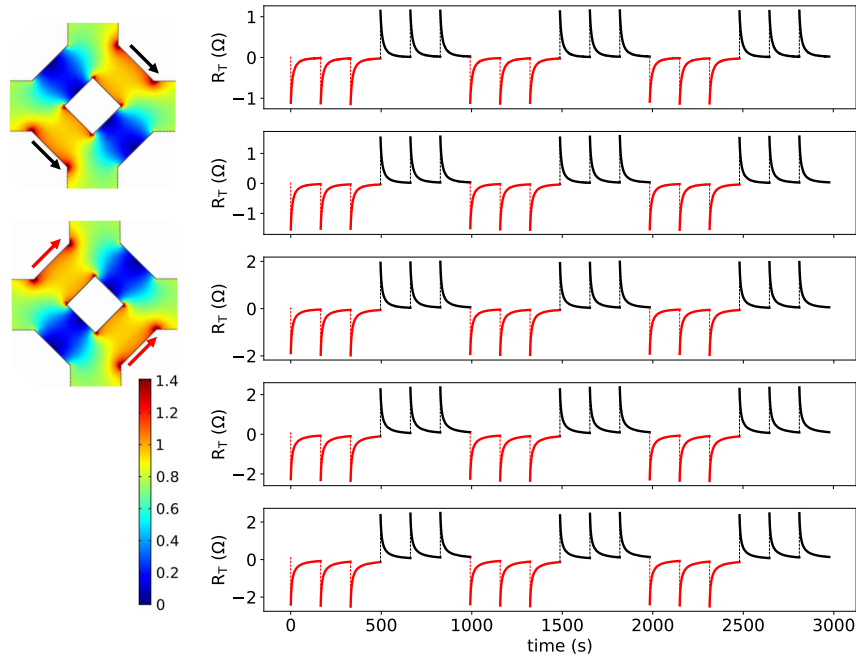


Figure 15: Same as Fig. 11 for the delay between pulses of 163 s.

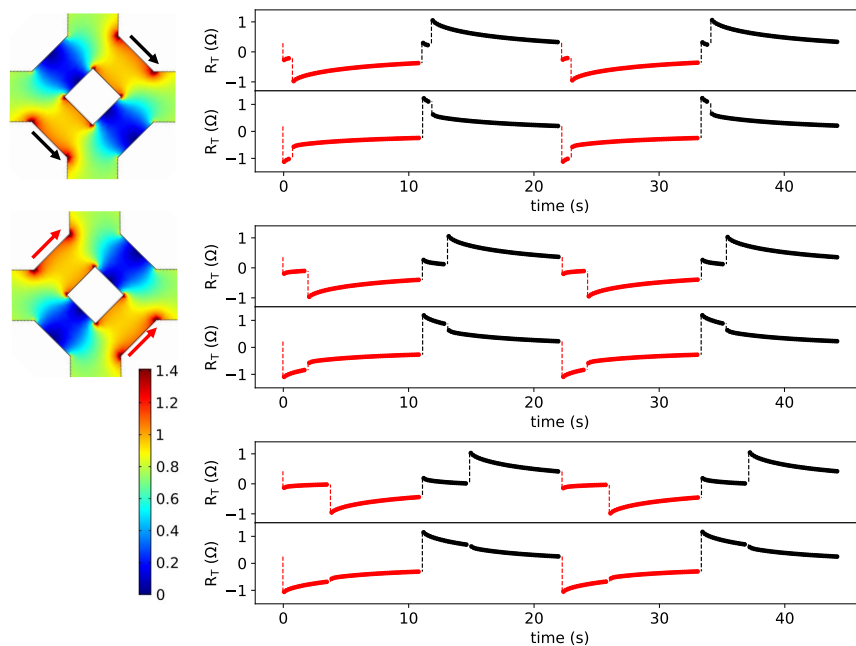


Figure 16: Each double-panel: A sequence of lower/higher (top panel) and higher/lower (bottom panel) pulses applied first along one pair of arms of the Wheatstone bridge (red arrows) and then along the other pair (black arrows). The measurement is repeated twice in each double-panel and the double-panels differ in the delay between the two pulses in the sequence. The experiments were done at room temperature.

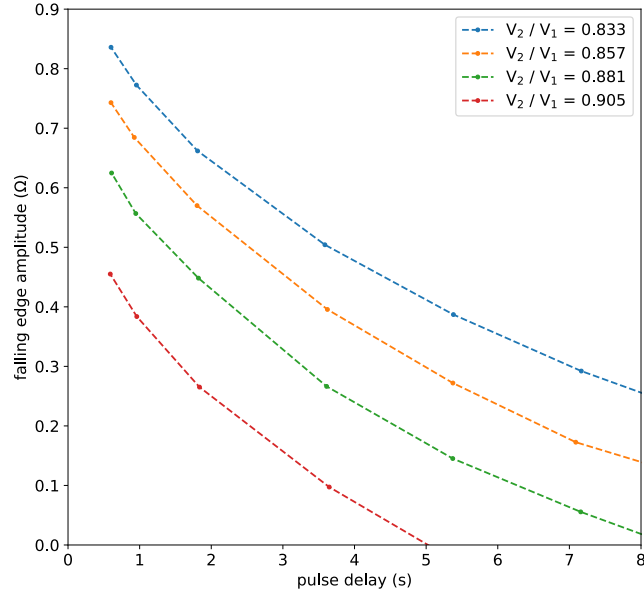


Figure 17: The dependence of the amplitude of the falling edge for the higher/lower sequence of pulses as a function of the pulse delay for different ratios of the writing voltage pulses applied in the Wheatstone device at room temperature.

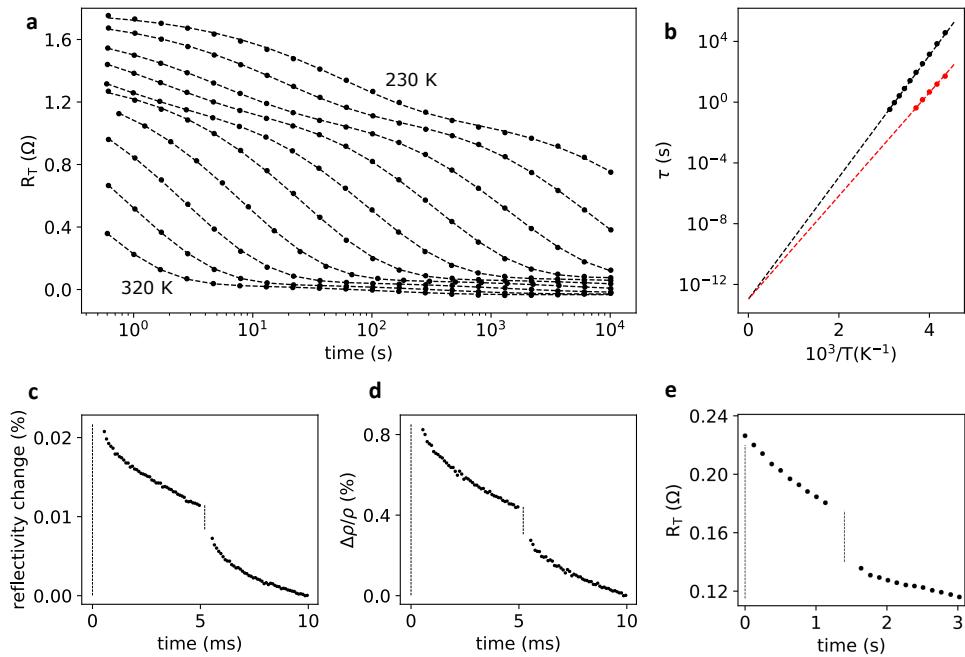


Figure 18: **a**, Time dependence of the relaxation of the switching signal in the Wheatstone-bridge device for temperatures ranging from 320 to 230 K (10 K step). Dashed lines are Kohlrausch stretched-exponential fits. **b**, Relaxation times  $\tau_{1(2)}$  inferred from fits in **a**, as a function of the inverse temperature. Dashed lines in **a,b** are fits; the extrapolated  $y$ -axis intercept in **b**, corresponds to the attempt time  $\tau_0$  and the slopes to the activation barriers  $E_{1(2)}$  (see text). **c,d** Comparison of optical reflectivity and electrical resistivity measurements of the same higher/lower electrical switching sequence. The measured millisecond-range relaxation at room temperature corresponds to the faster relaxing component ( $\tau_2$ ) from **a**. **e**, Room-temperature electrical detection of a higher/lower electrical switching sequence for 1 ns long pulses of amplitude 1.3 and  $1.1 \times 10^8 \text{ Acm}^{-2}$ , resp.

Another advantage of the Wheatstone-bridge geometry is that it removes the temperature depen-

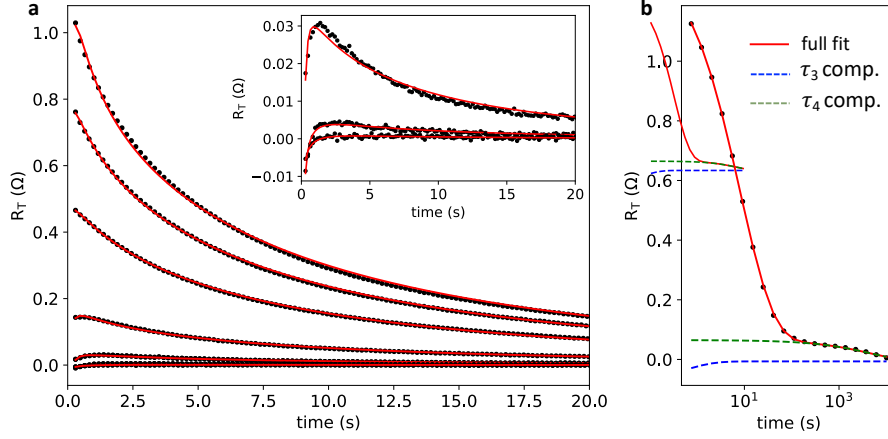


Figure 19: **a**, Stretched exponential fits and measured switching signals in the Wheatstone device at 290 K. From bottom to top, the curves correspond to pulse voltages 7.5–10.5 V. Inset: zoom-in for the voltages 7.5, 8, and 8.5 V highlighting the presence of an additional stretched-exponential component with a relaxation time  $\tau_3 = 0.3$  s at 290 K and an opposite sign to the two main components discussed in Fig. 3 of the main text. **b**, Data for the pulse voltage of 10.5 V for an enlarged and logarithmic time-scale highlighting the fourth stretched exponential component with  $\tau_4 = 620$  s at 290 K. The  $\tau_{3,4}$  components are much weaker than the leading components with  $\tau_{1,2}$  discussed in the main text.

dent offset resistance. (Without applying the switching pulse, the bridge is balanced and  $R_T = 0$ .) This allows us to perform low-noise measurements of the switching and subsequent relaxation over times spanning more than four orders of magnitude up to timescales of hours, as shown in Fig. 18a. The observed functional form of the relaxation is universal to all studied temperatures and contains two leading components accurately fitted to Kohlrausch stretched exponentials,  $\sim \exp[-(t/\tau_{1(2)})^\beta]$ , with  $\beta = 0.6$  and two different relaxation times. In theories of relaxation in complex systems, such as glassy materials,  $\beta = d/(d + 2)$  where  $d$  is the dimensionality of the diffusion equation describing the relaxation process [19]. Our experimental value of  $\beta$  corresponds to  $d = 3$  in the measured 50 nm thick film.

Consistent with theory [19], the dependence of the relaxation times on temperature follows a simple exponential,  $\tau_{1(2)} = \tau_0 \exp(E_{1(2)}/k_B T)$ , as seen in Fig. 18b. Here the extrapolated attempt time  $\tau_0$  is within the picosecond range typical of antiferromagnetic dynamics, compared to ferromagnets where it falls into the ns range [32]. For the activation energy we obtained  $E_1/k_B = 30.8 \times 300$  K for the slower component and  $E_2/k_B = 26.1 \times 300$  K for the faster component, giving the room-temperature relaxation times in the  $\sim 10$  s and  $\sim 10$  ms ranges, respectively. (For more details on the fitting see Fig. 19.) We point out that the exponential temperature dependence of the relaxation time explains the unipolar switching from the high to low resistivity state seen in Figs. 7 and 8. During the transient heating of the device due to the weaker pulse, the relaxation of the signal written by the preceding stronger pulse is exponentially accelerated which results in the abrupt falling edge of the signal after the weaker pulse. The resulting signal written by the weaker pulse is lower which reflects the dependence of the size of the signal on the amplitude of the writing pulse (cf. Fig. 7d).

The picture of switching in our devices into complex states, as described by the Kohlrausch model, is consistent with the antiferromagnetic domain nano-fragmentation systematically imaged in our devices by laboratory diamond magnetometry[14] and confirmed by our synchrotron X-ray microscopy – see Report 2.3. The Kohlrausch relaxation is an example, noted in the past in a range of physical systems, that reproducible and universal behavior can transcend the details of the complex disordered materials and of the measurement probes[19]. Indeed, we observe high reproducibility of the above switching and relaxation characteristics across different samples and experimental set-ups.

In Figs. 18c,d we demonstrate that our current-induced switching can be probed not only elec-

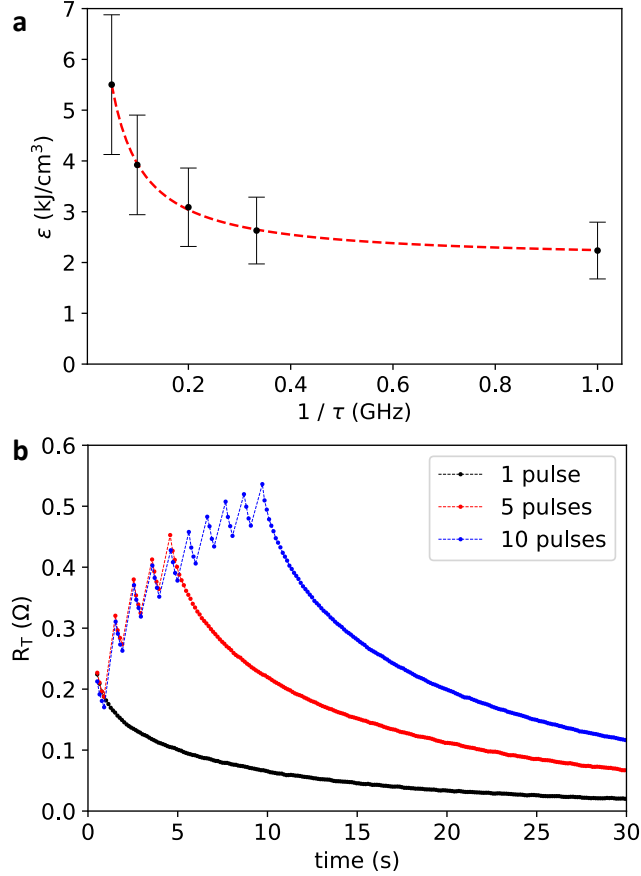


Figure 20: **a**, Joule heating energy density as a function of the switching speed  $1/\tau$  ( $\tau$  is the pulse length) measured on a  $5 \mu\text{m}$  wide bar device. The energy density is calculated from the current density ( $0.9 \times 10^8 \text{ Acm}^{-2}$  for  $\tau = 1 \text{ ns}$ ) and resistivity during the pulse. At  $200^\circ\text{C}$ , the resistivity increases by a factor of 3 compared to room temperature. The error bars correspond to the estimated temperature increase during the pulse of  $200 \pm 50^\circ\text{C}$ . Measurements are performed close to the switching threshold with the corresponding switching signal of 1%. For comparison, switching by the single 100 fs laser pulse of energy 1 nJ with the measured 30% absorption in the sample,  $1.7 \mu\text{m}$  spot size, and 50 nm film thickness (Fig. 4a of the main text) corresponds to energy density of  $2.6 \text{ kJcm}^{-3}$ . This is comparable to the saturated energy value for ns-electrical pulses. **b**, Switching signal after a single 1 ns pulse (black), and five (red) and ten (blue) 1 ns pulses of amplitude  $1.2 \times 10^8 \text{ Acm}^{-2}$ . The experiments were done at room temperature.

trically but also optically by measuring the reflectivity change. We again apply the stronger/weaker electrical writing pulse sequence and detect the falling edge. In this experiment we set the delay between the pulses to 5 ms to further illustrate the dynamics of the faster relaxing component ( $\tau_2$ ) of our switching signal. The short measurement window also allowed us to minimize the noise due to the optical set-up instability in the detection of the weak change in the optical reflectivity. Apart from the smaller amplitude, the optical signal (Fig. 18c) shows the same switching and relaxation pattern as the electrically detected signal (Fig. 18d).

### 4.3 Switching by ns-pulses

For consistency, we used  $100 \mu\text{s}$  writing pulses in all experiments presented so far. Our devices have, however, analogous switching characteristics over the full explored range of current pulse lengths down to 1 ns. This is illustrated in Fig. 18e, again on the stronger/weaker writing pulse sequence and the detection of the falling edge (for more results see Fig. 20b.). We point out that the writing current

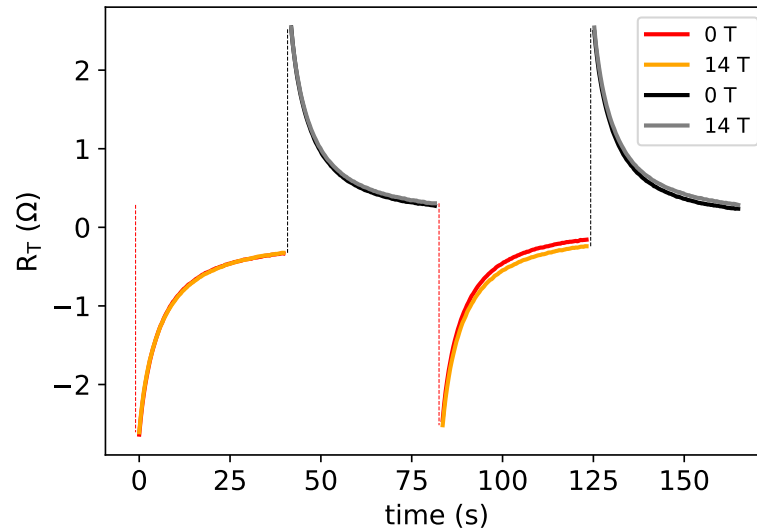


Figure 21: Comparison of the switching signal by  $100 \mu\text{s}$  pulses in the Wheatstone device measured at 0 and 14 T.

density in Fig. 18e is lower than in the spin-orbit torque switching in ferromagnetic devices by ns-pulses [18].

#### 4.4 Switching by strong magnetic fields

The large switching signals, ascribed to nano-fragmented multi-domain states, are insensitive to strong magnetic fields – see Fig. 21 for our measurements at 14 T.

## 5 Comparison of Whetstone-bridge and cross-shape bit-cells

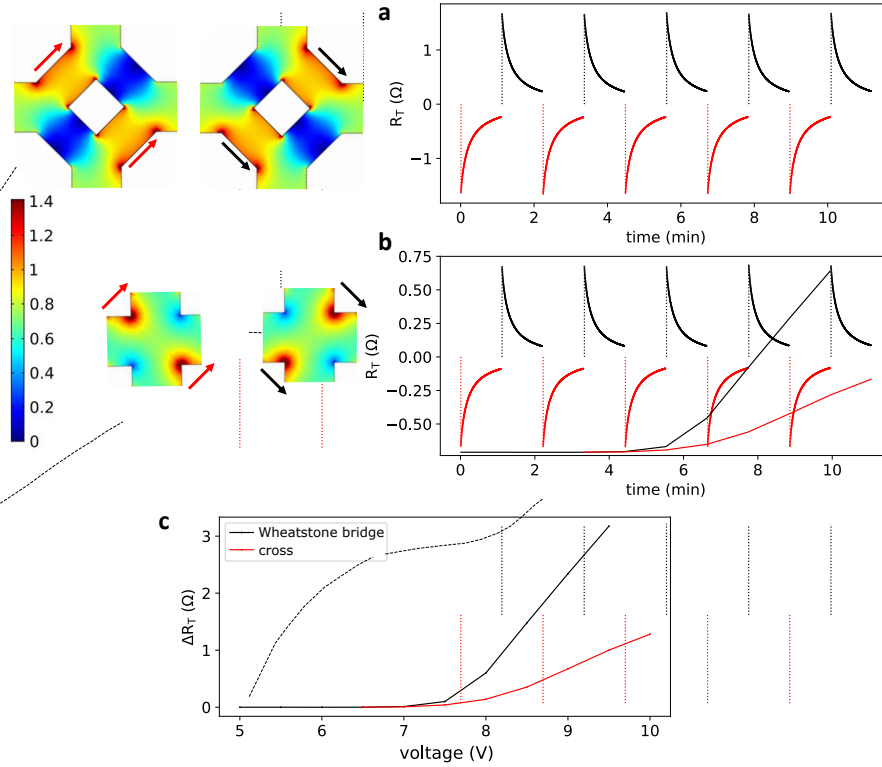


Figure 22: **a**, An example of the switching signal  $R_T$  measured on the Wheatstone bridge device for  $100 \mu s$ ,  $9.5 V$  pulses applied along one pair of arms (red arrows) and the orthogonal pair (black arrows). **b**, Analogous signal measured on a cross device for  $100 \mu s$ ,  $10 V$  pulses. Left panels: Comsol simulations of the writing current density maps. **c**, The amplitude of the switching signal as a function of the applied pulse voltage. In the Wheatstone bridge geometry, the amplitude of the signal can be directly related to the homogeneous change of the resistivity in the pulsed arms. In the cross geometry, the resistance change occurs primarily in the corners exposed to higher current density than the interior of the cross. As a result, the value of the signal observed in the cross geometry is significantly reduced because the readout electrical signal is effectively shunted by the central part of the device where switching is less efficient. From the experiment we estimate that the maximum achievable signal in simple cross geometry is approximately 40% of the value observed in the Wheatstone bridge for devices of size  $\sim 10 \mu m$ .

## References

- [1] Jungwirth, T., Marti, X., Wadley, P. & Wunderlich, J. Antiferromagnetic spintronics. *Nature Nanotechnology* **11**, 231–241 (2016). 1606.04284.
- [2] Železný, J., Wadley, P., Olejník, K., Hoffmann, A. & Ohno, H. Spin transport and spin torque in antiferromagnetic devices. *Nature Physics* **14**, 220–228 (2018).
- [3] Wadley, P. *et al.* Electrical switching of an antiferromagnet. *Science* **351**, 587–590 (2016). 1503.03765.
- [4] Olejník, K. *et al.* Antiferromagnetic CuMnAs multi-level memory cell with microelectronic compatibility. *Nature Communications* **8**, 15434 (2017).
- [5] Olejník, K. *et al.* Terahertz electrical writing speed in an antiferromagnetic memory. *Science Advances* **4**, eaar3566 (2018). URL <http://advances.sciencemag.org/lookup/doi/10.1126/sciadv.aar3566>. 1711.08444.
- [6] Šmejkal, L., Jungwirth, T. & Sinova, J. Route towards Dirac and Weyl antiferromagnetic spintronics. *physica status solidi (RRL) - Rapid Research Letters* **11**, 1700044 (2017). URL <http://doi.wiley.com/10.1002/pssr.201700044>. 1702.07788.
- [7] Šmejkal, L. & Jungwirth, T. Symmetry and topology in antiferromagnetic spintronics. In Zang, J., Cros, V. & Hoffmann, A. (eds.) *Topology in magnetism*, 267–298 (Springer International Publishing, 2018). URL <http://arxiv.org/abs/1804.05628>.
- [8] Šmejkal, L., González-Hernández, R., Jungwirth, T. & Sinova, J. Crystal Hall effect in Collinear Antiferromagnets. *arXiv:1901.00445* (2019). URL <https://lanl.arxiv.org/pdf/1901.00445><http://arxiv.org/abs/1901.00445>. 1901.00445.
- [9] Železný, J. *et al.* Relativistic néel-order fields induced by electrical current in antiferromagnets. *Physical Review Letters* **113**, 157201 (2014). 1410.8296.
- [10] Kašpar, Z. *et al.* High resistive unipolar-electrical and fs-optical switching in a single-layer antiferromagnetic memory 1–22 (2019). URL <http://arxiv.org/abs/1909.09071>. 1909.09071.
- [11] Wadley, P. *et al.* Current polarity-dependent manipulation of antiferromagnetic domains. *Nature Nanotechnology* **13**, 362–365 (2018). URL <http://www.nature.com/articles/s41565-018-0079-1>. arXiv:1711.05146.
- [12] Bodnar, S. Y. *et al.* Writing and reading antiferromagnetic Mn<sub>2</sub>Au by Néel spin-orbit torques and large anisotropic magnetoresistance. *Nature Communications* **9**, 348 (2018). URL <http://www.nature.com/articles/s41467-017-02780-x>. arXiv:1706.02482.
- [13] Wang, M. *et al.* Spin flop and crystalline anisotropic magnetoresistance in CuMnAs URL <http://arxiv.org/abs/1911.12381>. 1911.12381.
- [14] Wörnle, M. S. *et al.* Current-induced fragmentation of antiferromagnetic domains (2019). URL <http://arxiv.org/abs/1912.05287>. 1912.05287.
- [15] Chappert, C., Fert, A. & Van Dau, F. N. The emergence of spin electronics in data storage. *Nature Materials* **6**, 813–823 (2007). 1003.4058.
- [16] Máca, F. *et al.* Physical properties of the tetragonal CuMnAs: A first-principles study. *Physical Review B* **96**, 094406 (2017). 1708.06916.
- [17] Kimel, A. V. & Li, M. Writing magnetic memory with ultrashort light pulses. *Nature Reviews Materials* **4**, 189–200 (2019).

- [18] Baumgartner, M. *et al.* Spatially and time-resolved magnetization dynamics driven by spin-orbit torques. *Nature Nanotechnology* **12**, 980–986 (2017). URL <http://www.nature.com/doi/10.1038/nnano.2017.151>. arXiv:1704.06402v1.
- [19] Phillips, J. C. Axiomatic theories of ideal stretched exponential relaxation (SER). *Journal of Non-Crystalline Solids* **352**, 4490–4494 (2006).
- [20] Chiang, C. C., Huang, S. Y., Qu, D., Wu, P. H. & Chien, C. L. Absence of Evidence of Electrical Switching of the Antiferromagnetic Néel Vector. *Physical Review Letters* **123**, 227203 (2019). URL <https://link.aps.org/doi/10.1103/PhysRevLett.123.227203>.
- [21] Zink, B. The Heat in Antiferromagnetic Switching. *Physics* **12**, 134 (2019).
- [22] Zhang, P., Finley, J., Safi, T. & Liu, L. Quantitative Study on Current-Induced Effect in an Antiferromagnet Insulator/Pt Bilayer Film. *Physical Review Letters* **123**, 247206 (2019). URL <http://arxiv.org/abs/1907.00314>. 1907.00314.
- [23] Baldrati, L. *et al.* Mechanism of Néel Order Switching in Antiferromagnetic Thin Films Revealed by Magnetotransport and Direct Imaging. *Physical Review Letters* **123**, 177201 (2019). URL <http://arxiv.org/abs/1810.11326><https://link.aps.org/doi/10.1103/PhysRevLett.123.177201>. 1810.11326.
- [24] Cheng, Y., Yu, S., Zhu, M., Hwang, J. & Yang, F. Electrical Switching of Tristate Antiferromagnetic Néel Order in alpha Fe<sub>2</sub>O<sub>3</sub> Epitaxial Films. *Physical Review Letters* **124**, 027202 (2020). URL <http://arxiv.org/abs/1906.04694><https://link.aps.org/doi/10.1103/PhysRevLett.124.027202>. 1906.04694.
- [25] Churikova, A. *et al.* Non-magnetic origin of spin Hall magnetoresistance-like signals in Pt films and epitaxial NiO/Pt bilayers. *Applied Physics Letters* **116**, 022410 (2020). URL <http://aip.scitation.org/doi/10.1063/1.5134814>.
- [26] Kozlova, T., Rudneva, M. & Zandbergen, H. W. In situ TEM and STEM studies of reversible electromigration in thin palladium-platinum bridges. *Nanotechnology* **24**, 505708 (2013).
- [27] Krizek, F. *et al.* Molecular beam epitaxy of CuMnAs. *Physical Review Materials* **4**, 014409 (2020). URL <https://link.aps.org/doi/10.1103/PhysRevMaterials.4.014409>.
- [28] Kurenkov, A. *et al.* Artificial Neuron and Synapse Realized in an Antiferromagnet/Ferromagnet Heterostructure Using Dynamics of Spin-Orbit Torque Switching. *Advanced Materials* **31**, 1900636 (2019).
- [29] Wadley, P. *et al.* Tetragonal phase of epitaxial room-temperature antiferromagnet CuMnAs. *Nature Communications* **4**, 2322 (2013). 1402.3624.
- [30] Kriegner, D. *et al.* Multiple-stable anisotropic magnetoresistance memory in antiferromagnetic MnTe. *Nature Communications* **7**, 11623 (2016). 1508.04877.
- [31] Wadley, P. *et al.* Antiferromagnetic structure in tetragonal CuMnAs thin films. *Scientific Reports* **5**, 17079 (2015).
- [32] Aharoni, A. Effect of a Magnetic Field on the Superparamagnetic Relaxation Time. *Phys. Rev.* **177**, 793 (1969).